

Observation of metastability in open quantum dynamics of a solid-state system

Jun-Xiang Zhang,^{1,2,*} Yuan-De Jin,^{3,4,*} Chu-Dan Qiu,^{3,4} Wen-Long Ma,^{3,4,†} and Gang-Qin Liu^{1,5,‡}

¹*Beijing National Laboratory for Condensed Matter Physics and Institute of Physics,
Chinese Academy of Sciences, Beijing 100190, China*

²*School of Physical Sciences, University of Chinese Academy of Sciences, Beijing 100049, China*

³*State Key Laboratory of Superlattices and Microstructures,
Institute of Semiconductors, Chinese Academy of Sciences, Beijing, 100083, China*

⁴*Center of Materials Science and Opto-Electronic Technology,
University of Chinese Academy of Sciences, Beijing 100049, China*

⁵*Songshan Lake Materials Laboratory, Dongguan, Guangdong 523808, China*

(Dated: December 31, 2024)

Metastability is a ubiquitous phenomenon in non-equilibrium physics [1, 2] and classical stochastic dynamics [3, 4]. It arises when the system dynamics settles in long-lived states before eventually decaying to true equilibria. Remarkably, it has been predicted that quantum metastability can also occur in continuous-time [5] and discrete-time [6] open quantum dynamics. However, the direct experimental observation of metastability in open quantum systems has remained elusive. Here, we experimentally observe metastability in the discrete-time evolution of a single nuclear spin in diamond, realized by sequential Ramsey interferometry measurements of a nearby nitrogen-vacancy electron spin. We demonstrate that the metastable polarization of the nuclear spin emerges at around 60,000~250,000 sequential measurements, enabling high-fidelity single-shot readout of the nuclear spin under a small magnetic field of 108.4 gauss. An ultra-long spin relaxation time of more than 10 s has been observed at room temperature. By further increasing the measurement number, the nuclear spin eventually relaxes into the maximally mixed state. Our results represent a concrete step towards uncovering non-equilibrium physics in open quantum dynamics, which is practically relevant for the utilization of metastable information in various quantum information processing tasks [7, 8], such as accurate quantum operations [9, 10], quantum channel discrimination [11] and quantum error correction [12].

Introduction.— Metastability, similar to prethermalization in nonequilibrium physics [1], often emerges in classical or quantum many-body systems, when the system relaxes into long-lived states before subsequently decaying to true stationarity much slowly. In classical stochastic dynamics, metastability is a manifestation of a separation of time scales that arises from the splitting in the spectrum of the dynamical generator.

Recently quantum metastability theory has been extended to open quantum dynamics described by Markovian dynamics [5, 13, 14], where the manifold of metastable states is argued to be composed of disjoint states, decoherence-free subspaces, and noiseless subsystems. Such metastability theory is physically interesting from their own right and stimulates the prediction of metastability phenomena in various quantum models [15–23]. It is also of practical importance to utilize the preserved information of quantum processes for quantum information processing [7, 8], especially in the presence of control imperfections or environmental noise.

For the continuous-time dynamics described by the Lindblad master equation, metastability can be observed from the distinct two-step decay of temporal correlations [5]. However, experimental demonstrations remain scarce, mainly due to the difficulty of measuring temporal second-order or higher-order correlations with good resolution [24, 25]. Alternatively, certain signatures of metastability can be observed without measuring the

temporal correlations (e.g., through the high-accuracy time-resolved heterodyne detection in the superconducting cavities) [26], however, such approaches are generally not applicable to other experimental settings.

A recent advance in quantum metastability theory is the generalization of the setting from continuous-time to discrete-time open quantum dynamics [6]. Such a framework describes the more general scenario in which each discrete evolution is induced by a quantum channel (or a completely positive and trace-preserving quantum map) [27], which may not be generated by continuous-time master equations [28, 29]. With this framework, metastable open quantum dynamics of a quantum system can be directly observed by only sequentially measuring an ancilla qubit, instead of continuously measuring the temporal correlations. Remarkably, metastability has been predicted in the commonly-used Ramsey interferometry measurements (RIMs) [30–32], which is easy to realize in various quantum platforms. By repeating the RIM on a probe qubit, a nearby bath system can be metastably polarized, which is manifested in statistics of the probe measurement outcomes associated with different quantum trajectories of the bath system.

Here we report an observation of the metastable open dynamics in diamond based on sequential RIMs, using a nitrogen (¹⁴N) nuclear spin as the bath system and the nitrogen-vacancy (NV) electron spin as the probe. Due to the hyperfine coupling between the bath and the

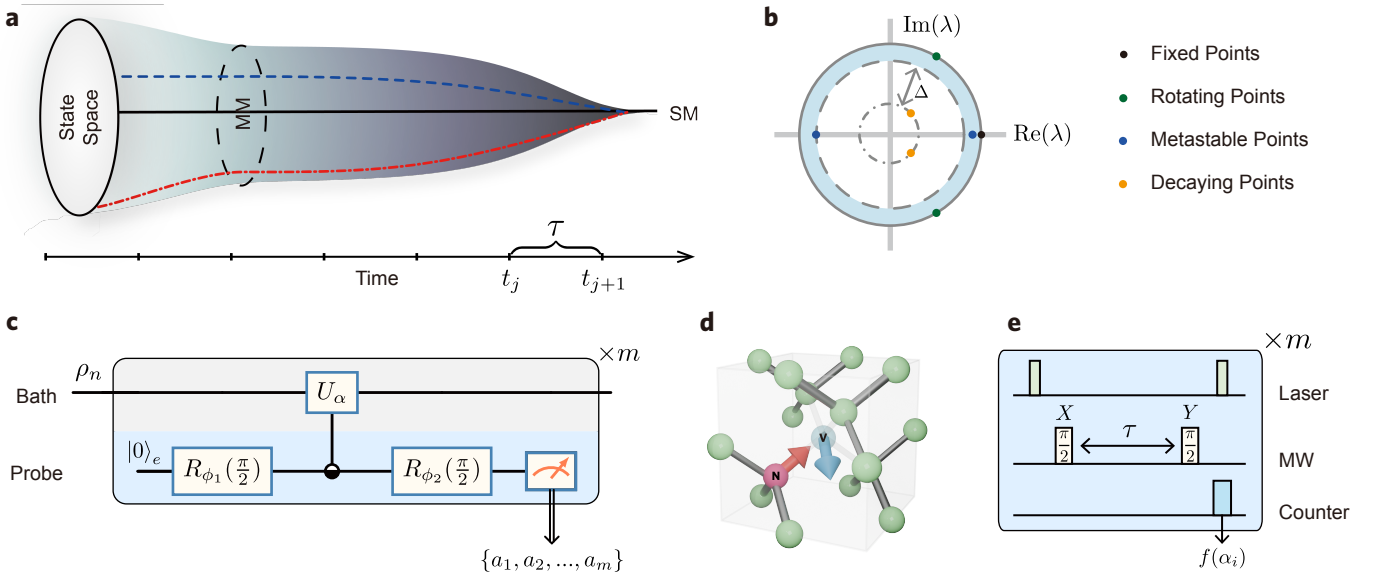


Figure 1. **Metastability in discrete-time open quantum dynamics and its observation in diamond.** **a**, Schematic of metastability in open quantum dynamics. The states outside the metastable manifold (MM, red dot-dashed line) exhibit a two-step relaxation, i.e., first quickly relaxing into the MM and then slowly decaying into the stationary manifold (SM). The discrete-time axis implies that the open quantum dynamics is described by sequential quantum channels. **b**, Spectrum of a quantum channel, with all eigenvalues (solid circles) located within the unit circle of the complex plane. Metastable points emerge in the region $|\lambda| \approx 1$ (labeled with blue ring in the spectrum). The range of metastable region is determined by the spectral gap Δ between the decaying point with the largest eigenvalue (dot-dashed circle) and the metastable point with the smallest eigenvalue (dashed circle). **c**, Quantum circuit of sequential RIMs, where $R_\phi(\theta)$ is the rotation operator of the probe qubit, U_α is a unitary operator of the bath conditioned on the probe state $|\alpha\rangle_e$ ($\alpha = 0, 1$), and $\{a_1, \dots, a_m\}$ is the sequence of measurement outcomes. **d**, The experimental system, with the electron spin of a nitrogen-vacancy (NV) center serving as the probe qubit, and the host ^{14}N nuclear spin as the quantum bath system. **e**, Pulse sequences to implement sequential RIMs in experiments. Laser pulses are used to polarize and read out the NV spin state, and resonant microwave pulses are used to manipulate the probe spin state.

probe during free evolution, each round of RIM solely applied on the probe spin induces a quantum channel on the nuclear spin, and sequential RIMs induce discrete-time open quantum dynamics on the nuclear spin (Fig. 1a). By recording the statistical results of the sequential probe measurement, we can continuously monitor the state evolution of the target spin. We directly observe the metastable polarization with varying the number of repetitions m , i.e., the bath spin is first steered to metastable (polarized) states for a finite range of m , and eventually relaxes towards the true stable (maximally mixed) state as m continues to increase.

Metastability in sequential RIMs.— We illustrate the principle of metastability by considering a typical class of sequential quantum channels on a quantum bath system, with the channel being induced by a probe qubit under a RIM sequence [6]. The probe qubit is coupled to the bath through the general pure-dephasing coupling

$$H = \sigma_e^z \otimes B_n + \mathbb{I}_e \otimes C_n, \quad (1)$$

where the subscripts e and n refer to the probe and bath respectively, σ_e^i is the Pauli- i operator of the qubit ($i = x, y, z$) with $\sigma_e^z = |0\rangle_e\langle 0| - |1\rangle_e\langle 1|$, and B_n (C_n) is

the interaction (free) operator of the bath. We denote the qubit rotation along an axis in equatorial plane as $R_\phi(\theta) = e^{-i(\cos \phi \sigma_q^x + \sin \phi \sigma_q^y)\theta/2}$, with ϕ denoting the rotation axis and θ the rotation angle.

For a single RIM, the qubit is first initialized to state $|0\rangle_e$, and then prepared in a superposition state $|\psi\rangle_e = (|0\rangle_e - ie^{i\phi_1}|1\rangle_e)/\sqrt{2}$ by a rotation $R_{\phi_1}(\pi/2)$. After the composite system evolving with the pure-dephasing coupling [Eq. (1)] for time τ , the qubit undergoes another rotation $R_{\phi_2}(\pi/2)$, and is finally projectively measured in the basis of σ_e^z with the measurement outcome $a \in \{0, 1\}$.

The RIM sequence of the probe spin induces a quantum channel Φ on the bath,

$$\Phi(\rho_n) = \text{Tr}_e [U(\rho_e \otimes \rho_n)U^\dagger] = \sum_{a=0,1} M_a \rho_n M_a^\dagger, \quad (2)$$

where $\rho_e = |\psi\rangle_e\langle\psi|$ (ρ_n) is the initial state of the probe (bath) spin, $U = e^{-iH\tau}$ is the propagator for the composite system. By partially tracing over the probe spin, we obtain the Kraus operator $M_a = [U_0 - (-1)^a e^{i\Delta\phi} U_1]/2$ with $U_\alpha = e^{-i[(-1)^\alpha B_n + C_n]\tau}$ and $\Delta\phi = \phi_1 - \phi_2$ being the phase difference between the rotation axes of two $\pi/2$ pulse in RIMs. While obtaining the outcome a ,

the bath state is steered to $M_a \rho_n M_a^\dagger$ with probability $p(a) = \text{Tr}(M_a \rho_n M_a^\dagger)$. Note that $\sum_a M_a^\dagger M_a = \mathbb{I}$ ensures that $\sum_a p(a) = 1$.

The behaviors of repetitive quantum channels can be clearly revealed by the spectral decomposition of a single channel (see Method). A quantum channel has at least one fixed point (Fig. 1b), which is the state that remains unchanged after the channel [33, 34]. It has been proved that the fixed points depend on the commutativity of B_n and C_n (see Method). If B_n commutes with C_n , i.e., $[B_n, C_n] = 0$, the fixed points are the simultaneous eigenstates of B_n and C_n , then sequential RIMs of the probe spin will polarize the bath system to one of the eigenstates, also constituting a quantum non-demolition (QND) measurement on the bath spin [35–37]. However, if $[B_n, C_n] \neq 0$, the fixed points are the maximally mixed state in the whole space (or subspace) of the bath, then sequential RIMs cannot effectively measure the bath system but only perturb it.

Quantum metastability emerges when $[B_n, C_n] \neq 0$, but C_n is a small perturbation of B_n , then the bath will be polarized for a finite range of repetitions of RIMs. We suppose that the channel has r fixed points and $q - r$ metastable points, which collectively span a $(q - 1)$ -dimensional metastable manifold (MM). The metastable region of the polarization of the whole state space can be estimated as $(1 - |\lambda_{q+1}|)^{-1} \ll m \ll (1 - |\lambda_q|)^{-1}$ when λ_q is very close to 1, where λ_q is the eigenvalue of metastable point with the smallest eigenvalue. As m increases and enters the metastable region, the system's state evolves into the MM. Beyond this region, the system further relaxes into the stationary manifold (SM), which is spanned by the fixed points. This process, where the system first reaches the MM and then relaxes to the SM, is referred to as a two-step relaxation (see Fig. 1a).

The metastability behaviors in sequential RIMs can be directly monitored by the measurement statistics of the probe spin [6]. To see this, we decompose the average dynamics of sequential quantum channels into stochastic trajectories,

$$\Phi^m(\rho_n) = \sum_{a_1, \dots, a_m=0}^1 \mathcal{M}_{a_m} \cdots \mathcal{M}_{a_1}(\rho_n), \quad (3)$$

where $\mathcal{M}_{a_i}(\cdot) = M_{a_i}(\cdot)M_{a_i}^\dagger$ with $a_i \in \{0, 1\}$ being the measurement outcome of the i th RIM. For a trajectory with the sequence of measurement outcomes $\{a_1, \dots, a_m\}$, the bath is steered to $\rho'_n = \mathcal{M}_{a_m} \cdots \mathcal{M}_{a_1}(\rho_n)/p(a_1, \dots, a_m)$ with probability $p(a_1, \dots, a_m) = \text{Tr}[\mathcal{M}_{a_m} \cdots \mathcal{M}_{a_1}(\rho_n)]$. For a trajectory with $\{a_1, \dots, a_m\}$ with the number of outcome 0/1 being m_0/m_1 ($m_0 + m_1 = m$), we define the measurement polarization $X = (m_0 - m_1)/(2m)$, denoting the different classes of stochastic trajectories that the target system undergoes. The measurement distribution of X can show several peaks, with each peak corresponding to

the quantum trajectories that lead to a fixed point (or metastable state) of the channel (see Methods). So in the metastable region, the distribution exhibits up to q peaks, corresponding to the metastable states. However, as m surpasses this region, the number of peaks gradually reduces to r , reflecting the final stationary states of the bath.

Experimental implementation in the NV system.— We demonstrate this protocol experimentally on an NV center and a nearby nuclear spin in a high-purity diamond (Fig. 1d). Nuclear spins around NV centers have great potential for building quantum networks [38], storing quantum information [39], establishing quantum simulator [40–42], sensing inertial parameters [43], and so on. Access to the nuclear spins is usually based on their hyperfine interaction with the electron spin and the optical interface of the NV center. It is therefore an interesting and fundamental problem to monitor and understand the dynamics of these nuclear spins under multiple measurements acting on the central electron spin.

Specifically, an NV electron spin is a spin-1 system with a zero-field splitting $D = 2.87$ GHz between its $|0\rangle_e$ ($m_s = 0$) and $|\pm 1\rangle_e$ ($m_s = \pm 1$) state. In our experiment, a moderate external magnetic field of $B = 108.4 \pm 0.2$ G is applied along the NV symmetry axis (z axis) to lift the degeneracy of the $|\pm 1\rangle_e$ states and we work in the $\{|0\rangle_e, |-1\rangle_e\}$ subspace. The Hamiltonian in Eq. (1) becomes (in the rotating frame)

$$H = A_{zz}S_zI_z + QI_z^2 - \gamma_n \mathbf{B} \cdot \mathbf{I} + \tilde{H}_1, \quad (4)$$

where S_z (I_z) is Pauli- z operator for the NV electron spin (^{14}N nuclear spin) with $\mathbf{I} = (I_x, I_y, I_z)$, $A_{zz} = -2.16$ MHz ($A_\perp = -2.63$ MHz) is the zz -component (transverse component) of the hyperfine tensor, $Q = -4.95$ MHz is the quadrupolar splitting, γ_n (γ_e) being the gyromagnetic ratio of ^{14}N nuclear spin (electron spin), and $\tilde{H}_1 = \sum_\alpha |\alpha\rangle_e \langle \alpha| \otimes H_n^\alpha$ is a second-order perturbation term with $H_n^\alpha \approx \frac{\gamma_e(2-3|\alpha|)}{2D} [-\gamma_e(B_x^2 + B_y^2) + 2A_\perp(B_xI_x + B_yI_y)]$. To introduce a non-commutativity between $B_n = A_{zz}I_z$ and $C_n = QI_z^2 - \gamma_n \mathbf{B} \cdot \mathbf{I} + \tilde{H}_1$, the external magnetic field is slightly misaligned with the NV axis. Under this circumstance, the perturbation terms $-\gamma_n(B_xI_x + B_yI_y)$ and \tilde{H}_1 lead to the metastable polarization of ^{14}N .

For each RIM, the resulting quantum state of the NV spin is read out by counting its spin-dependent photon number. As shown in Fig. 1e, a 532-nm laser is used to excite the NV center and all experiments are performed at room temperature. Due to the low photon emission rate of the single NV center and the short readout time (200 ns, see discussion below), on average only 0.05 photons can be detected in each measurement. To obtain a reasonable signal-to-noise ratio, we simply sum the counts of many measurements. The relatively low readout efficiency of the NV electron spin corresponds to a weak measurement of the electron spin (see Methods),

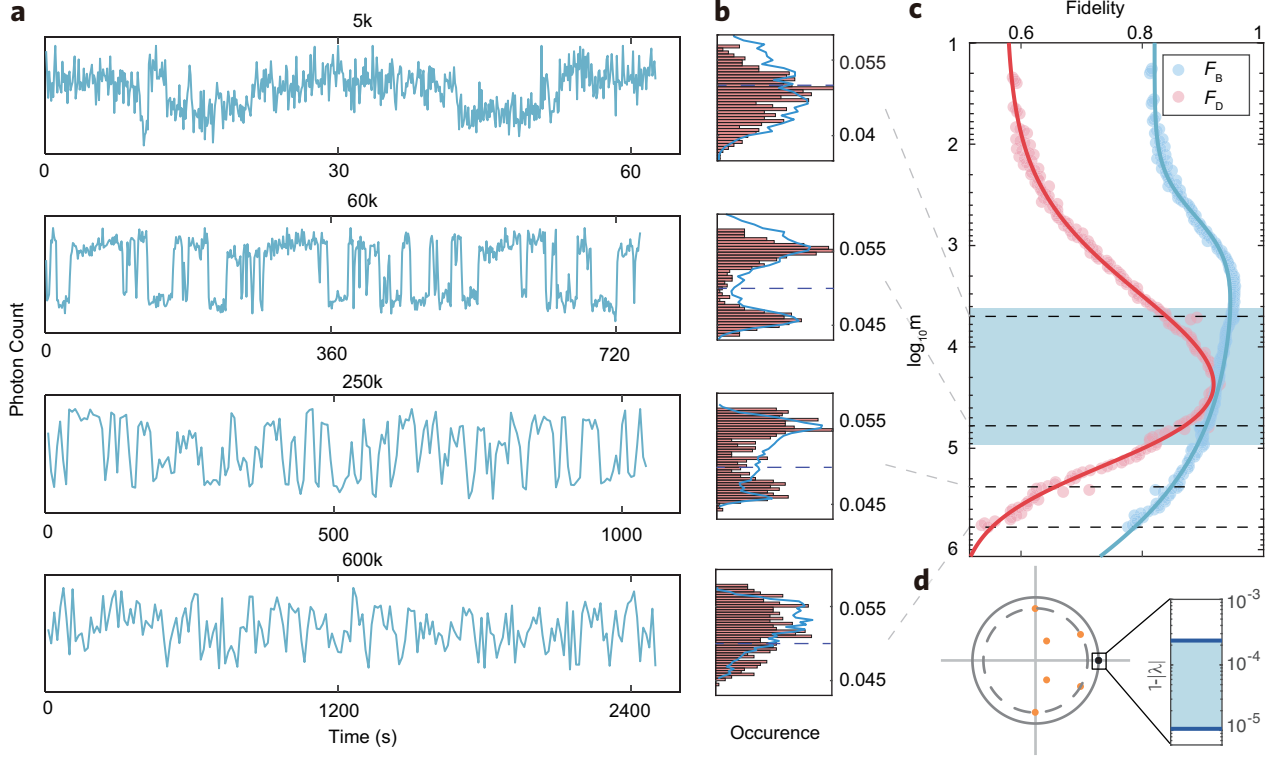


Figure 2. **Metastable dynamics of a ^{14}N nuclear spin induced by sequential RIMs of a nearby NV electron spin.** **a-b**, Typical PL time trace of an NV center under sequential RIMs and distribution of consecutive measurements. The duration of free evolution, $\tau = 374$ ns. The number of measurement repetition, m , is 5 k, 60 k, 250 k, 600 k, from top to bottom, respectively. At a relatively small $m = 5$ k, it is difficult to distinguish the nuclear spin quantum states. Increasing m to 60 k results in the jump signal being concentrated in two distinct photon count intervals. As m increase further to 250 k, the overlap between the two distribution peaks becomes more pronounced. When m exceeds the metastable region, the photon counting peaks gradually merge as m continues to increase. The blue envelopes indicate the normalized numerical simulation results. **c**, The evolution of fidelity for quantum trajectories in the numerical simulation of sequential RIMs. The initial thermal state evolves through metastable dynamics: trajectories are polarized to either the dark state ($|1\rangle_n$) or the bright state, represented by the subspace spanned by $|0\rangle_n$ and $|-1\rangle_n$. The fidelity $F_{D,B}$ quantifies how close the quantum states represented by the trajectories are to the ideal dark or bright states, respectively. **d**, The channel spectrum, with one fixed point, two metastable points and six decaying points, the absolute value of metastable points are shown in right. The metastable region after the relaxation of λ_3 and before that of λ_2 is labeled with blue shade in **c** and **d**. Monte Carlo simulations are conducted with a tilt angle $\theta = 8.8^\circ$ and 3000 samples.

which make it more challenging to observe metastable polarization of the nuclear spin. We anticipate that such metastable polarization can be more efficiently realized with projective (strong) measurement of the NV electron spin [44, 45].

Figure 2 presents the metastable dynamics of the target nuclear spin under sequential RIMs acting on the NV electron spin. Before the measurement, the ^{14}N nuclear spin is in the thermal state, which means that its population is evenly distributed among the set of states $\{|0\rangle_n, |\pm 1\rangle_n\}$ ($m_I = 0, \pm 1$). For a small number of RIMs ($m < 5\text{ k}$), the shot-noise of the photon counts exceeds the count difference of the states to-be resolved (the signal), so that no signal can be detected in this range. As the number of RIMs increased, the measurement results

begin to concentrate on two regions, a clear signature of the metastable polarization of the bath spin, as can be seen in the middle slice of Fig. 2a,b. We classify the trajectories based on the average photon number with a threshold of 0.05. If the average photon number is less than 0.05, it is classified as a *dark* state, otherwise as a *bright* state. Since the ^{14}N nuclear spin is a three-level system, three peaks are expected, and the feature of only two peaks indicates that two of them cannot be distinguished through current weak measurements of the electron spin. Through numerical simulations (see Extended Data Fig. 2 c), we find that three peaks are observed at about 5 k measurements and two of them are depolarized before 60 k measurements. For the measurement number of ($m > 5\text{ k}$), the experimentally resolved bright state

corresponds to the projector of the subspace spanned by $|0\rangle_n$ and $|-1\rangle_n$. This projector, together with $|1\rangle_n$ (dark state), are the extremely metastable states (EMSs) of the one-dimensional MM spanned with the fixed point and the metastable point with higher eigenvalue of the quantum channel. Beyond the metastable region ($m > 600$ k), the two peaks mentioned above gradually disappear and a single peak appears, which corresponds to the stable state of the system. More data can be found in Extended data Figs. 1 and 2.

To quantitatively understand the metastable dynamics of the nuclear spin, we perform numerical simulations that take into account the parameters of hyperfine coupling, the strength of the external magnetic field and the readout efficiency of the NV electron spin. The metastable states can be quantified by comparing them with the ideal polarization states, $\rho_D = |1\rangle_n\langle 1|$ for the *dark* state and the projector $\rho_B = (|0\rangle_n\langle 0| + |-1\rangle_n\langle -1|)/2$ for the *bright* state. In particular, their evolution fidelities are calculated as $F_{D(B)} = F(\rho_{D(B)}, \rho_n)$, where the fidelity $F(\rho, \sigma) = \text{Tr} \sqrt{\rho^{1/2} \sigma \rho^{1/2}}$ and ρ_n is the state of the specific trajectory. As shown in Fig. 2c, the experimentally observed metastable dynamics of the ^{14}N can be well reproduced with a tilted angle of the magnetic field of $\theta = 8.8^\circ$. By choosing a smaller angle of the external magnetic field, the metastable stage of all three polarized nuclear spin states with $m_I = 0, \pm 1$ can last for a long time, which enabling the observation of three-peak jumps in the experiment, see Extended Data Fig. 3 for details.

Single-shot readout of a single nuclear spin— The observed metastability provides a simple and efficient way to realize high-fidelity single-shot readout of the nuclear spin. Under a magnetic field tilted angle $\theta = 7^\circ \pm 2^\circ$ and a RIM interval of $\tau = 374$ ns, the quantum jumps of the nuclear spin are clearly observed in the measurement number range from 5 k to 250 k. We then characterize the readout fidelity of the nuclear spin using the method developed in [46, 47], and the results are summarized in Fig. 3a. It is worth noting that both the external magnetic field and the RIM interval affect the occurrence of the metastable states, so as to the optimal readout region, as shown in Fig. 3a. With a repetition number of $m = 80$ k (total measurement time 1.73 s), a readout fidelity of $97\% \pm 2\%$ with a threshold count value of 2950 is achieved.

Next, we investigate the relaxation mechanism of the ^{14}N nuclear spin under repeated measurements. Previous studies have shown that the flip-flop process in the excited state of the NV center is the dominant factor, and usually a large external magnetic field (> 2000 G) is applied to suppress this term so that single-shot readout of the nuclear spin can be achieved [46, 48]. Alternatively, our results show that the nuclear spin relaxation can be largely suppressed by simply shortening the duration of

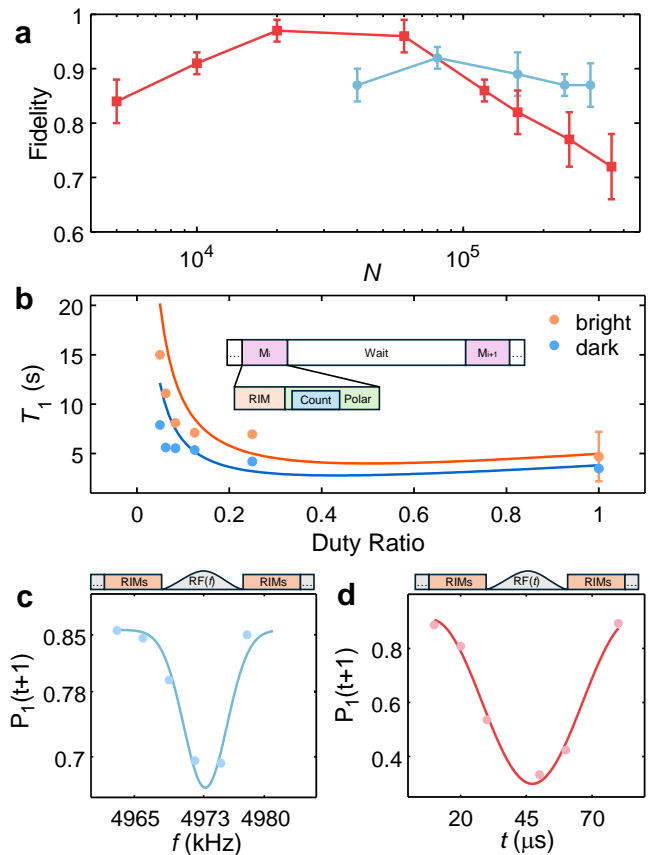


Figure 3. Single-shot readout of the nuclear spin state.

a, Readout fidelity of the ^{14}N nuclear spin as a function of the measurement repetition number. The data points with $\theta = 7^\circ \pm 2^\circ$, $\tau = 374$ ns are shown in red squares, while the data points with $\theta = 7^\circ \pm 2^\circ$, $\tau = 370$ ns are shown in blue circles. **b**, ^{14}N nuclear spin relaxation time (bright state in orange and dark state in blue) as a function of the duty cycle of the excitation laser pulses. The inset illustrates the experimental pulse sequence. The duty cycle is defined as the ratio of the measurement time to the waiting time in the sequence. **c**, ^{14}N nuclear spin NMR, obtained by varying the radio-frequency (RF) pulse frequency at a fixed pulse duration of 30 μs . **d**, ^{14}N nuclear spin Rabi oscillations. A resonant RF pulse of a specific length is applied between every two sequential RIMs to flip the nuclear spin between the $|0\rangle_n$ and $|+1\rangle_n$ states, while the electron is at the $|0\rangle_n$ state.

the excitation laser. Moreover, by inserting additional waiting intervals between the sequential RIMs, a longer nuclear spin T_1 is observed, as summarized in Fig. 3b. The longest T_1 measured in our experiment is 15 s.

Finally, we perform nuclear magnetic resonance (NMR) and Rabi measurements to demonstrate the coherent control of the ^{14}N nuclear spin. The nuclear spin state is first prepared by a RIM measurement sequence (either in the bright or dark state), then a RF pulse is applied to flip the nuclear spin, and a second RIM measurement is performed to determine the nuclear spin state. The RF pulse is either fixed in duration ($30\text{ }\mu\text{s}$ for NMR)

or fixed in frequency (resonant frequency for Rabi). The sequence are repeated for 80 k times and the probability of nuclear spin flip are recorded. As mentioned above, the experimentally resolved bright state corresponds to the maximally mixed state in the subspace $\{|0\rangle_n, |-1\rangle_n\}$, so we fit the fluorescence time trace using a three-state hidden Markov model. Fig. 3c shows the NMR signal at 4973.0 kHz, which corresponds to the ^{14}N -bath nuclear spin being in $|+1\rangle_n$ state. Fig. 3d shows the Rabi oscillation of the ^{14}N nuclear spin between the states $|+1\rangle_n$ and $|0\rangle_n$. These results further confirm the observed quantum jump signal originating from the ^{14}N nuclear spin.

Conclusion and outlook.—In conclusion, we have directly observed metastability in the discrete-time open quantum dynamics of a single nuclear spin in diamond, induced by sequential RIMs of a probe NV electron spin. The observed metastable polarization of the nuclear spin is of practical importance for constructing QND measurements of a quantum system that can be easily extended to other physical platforms, including trapped-ions, superconducting circuits, and other semiconductor single-spin systems. On the other hand, our results also point to a potential issue in constructing quantum networks with NV centers or other single-spin systems, since sequential measurements of an ancilla can cause its nearby memory to equilibrate towards a maximally mixed state, leading to the loss of information about the stored state.

The generality of our protocols is also a blueprint for future studies of non-equilibrium phenomena in open quantum systems. It will be interesting to realize more general channels in both theory and experiments in the future, whose fixed points may include decoherence-free subspaces or noise-free subsystems, and to explore the metastability phenomena for protected coding and logical gates. Such phenomena can be directly relevant to quantum information processing, since the fixed points of a quantum channel with preserved information can become metastable when control errors or environmental noise are taken into account.

* These authors contributed equally to this work

† wenlongma@semi.ac.cn

‡ gqliu@iphy.ac.cn

- [1] T. Mori, T. N. Ikeda, E. Kaminishi, and M. Ueda, Thermalization and prethermalization in isolated quantum systems: a theoretical overview, *Journal of Physics B: Atomic, Molecular and Optical Physics* **51**, 112001 (2018).
- [2] C.-J. Lin, A. Chandran, and O. I. Motrunich, Slow thermalization of exact quantum many-body scar states under perturbations, *Phys. Rev. Res.* **2**, 033044 (2020).
- [3] B. Gaveau and L. S. Schulman, Dynamical metastability, *J. Phys. A* **20**, 2865 (1987).
- [4] B. Gaveau and M. Moreau, Metastable relaxation times and absorption probabilities for multidimensional

- stochastic systems, *J. Phys. A* **33**, 4837 (2000).
- [5] K. Macieszczak, M. Guță, I. Lesanovsky, and J. P. Garrahan, Towards a theory of metastability in open quantum dynamics, *Phys. Rev. Lett.* **116**, 240404 (2016).
- [6] Y.-D. Jin, C.-D. Qiu, and W.-L. Ma, Theory of metastability in discrete-time open quantum dynamics, *Phys. Rev. A* **109**, 042204 (2024).
- [7] R. Blume-Kohout, H. K. Ng, D. Poulin, and L. Viola, Characterizing the structure of preserved information in quantum processes, *Phys. Rev. Lett.* **100**, 030501 (2008).
- [8] R. Blume-Kohout, H. K. Ng, D. Poulin, and L. Viola, Information-preserving structures: A general framework for quantum zero-error information, *Phys. Rev. A* **82**, 062306 (2010).
- [9] S. Ma, G. Liu, P. Peng, B. Zhang, S. Jandura, J. Claes, A. P. Burgers, G. Pupillo, S. Puri, and J. D. Thompson, High-fidelity gates and mid-circuit erasure conversion in an atomic qubit, *Nature* **622**, 279 (2023).
- [10] N. Earnest, S. Chakram, Y. Lu, N. Irons, R. K. Naik, N. Leung, L. Ocola, D. A. Czaplewski, B. Baker, J. Lawrence, J. Koch, and D. I. Schuster, Realization of a Λ system with metastable states of a capacitively shunted fluxonium, *Phys. Rev. Lett.* **120**, 150504 (2018).
- [11] K. DeBry, J. Sinanan-Singh, C. D. Bruzewicz, D. Reens, M. E. Kim, M. P. Roychowdhury, R. McConnell, I. L. Chuang, and J. Chiaverini, Experimental quantum channel discrimination using metastable states of a trapped ion, *Phys. Rev. Lett.* **131**, 170602 (2023).
- [12] M. Kang, W. C. Campbell, and K. R. Brown, Quantum error correction with metastable states of trapped ions using erasure conversion, *PRX Quantum* **4**, 020358 (2023).
- [13] K. Macieszczak, D. C. Rose, I. Lesanovsky, and J. P. Garrahan, Theory of classical metastability in open quantum systems, *Phys. Rev. Research* **3**, 033047 (2021).
- [14] C. A. Brown, K. Macieszczak, and R. L. Jack, Unraveling metastable markovian open quantum systems, *Phys. Rev. A* **109**, 022244 (2024).
- [15] D. C. Rose, K. Macieszczak, I. Lesanovsky, and J. P. Garrahan, Metastability in an open quantum Ising model, *Phys. Rev. E* **94**, 052132 (2016).
- [16] A. Le Boité, M.-J. Hwang, and M. B. Plenio, Metastability in the driven-dissipative Rabi model, *Phys. Rev. A* **95**, 023829 (2017).
- [17] Z. Gong, R. Hamazaki, and M. Ueda, Discrete time-crystalline order in cavity and circuit QED systems, *Phys. Rev. Lett.* **120**, 040404 (2018).
- [18] F. M. Gambetta, F. Carollo, M. Marcuzzi, J. P. Garrahan, and I. Lesanovsky, Discrete time crystals in the absence of manifest symmetries or disorder in open quantum systems, *Phys. Rev. Lett.* **122**, 015701 (2019).
- [19] H. Landa, M. Schiró, and G. Misguich, Multistability of Driven-Dissipative Quantum Spins, *Phys. Rev. Lett.* **124**, 043601 (2020).
- [20] V. P. Flynn, E. Cobanera, and L. Viola, Topology by dissipation: Majorana bosons in metastable quadratic markovian dynamics, *Phys. Rev. Lett.* **127**, 245701 (2021).
- [21] Nicolò Defenu, Metastability and discrete spectrum of long-range systems, *Proc. Natl. Acad. Sci.* **118**, e2101785118 (2021).
- [22] S. B. Jäger, T. Schmit, G. Morigi, M. J. Holland, and R. Betzholz, Lindblad master equations for quantum systems coupled to dissipative bosonic modes, *Phys. Rev.*

- Lett. **129**, 063601 (2022).
- [23] A. Cabot, F. Carollo, and I. Lesanovsky, Metastable discrete time-crystal resonances in a dissipative central spin system, *Phys. Rev. B* **106**, 134311 (2022).
 - [24] M. Fitzpatrick, N. M. Sundaresan, A. C. Y. Li, J. Koch, and A. A. Houck, Observation of a dissipative phase transition in a one-dimensional circuit qed lattice, *Phys. Rev. X* **7**, 011016 (2017).
 - [25] F. Letscher, O. Thomas, T. Niederprüm, M. Fleischhauer, and H. Ott, Bistability versus metastability in driven dissipative rydberg gases, *Phys. Rev. X* **7**, 021020 (2017).
 - [26] G. Beaulieu, F. Minganti, S. Frasca, V. Savona, S. Felicetti, R. Di Candia, and P. Scarlino, Observation of first-and second-order dissipative phase transitions in a two-photon driven kerr resonator, *arXiv preprint arXiv:2310.13636* (2023).
 - [27] J. Watrous, *The Theory of Quantum Information* (Cambridge university press, 2018).
 - [28] S. Gudder, Quantum Markov chains, *J. Math. Phys.* **49**, 072105 (2008).
 - [29] D. Amato, P. Facchi, and A. Konderak, Asymptotics of quantum channels, *J. Phys. A: Math. Theor.* **56**, 265304 (2023).
 - [30] N. F. Ramsey, A molecular beam resonance method with separated oscillating fields, *Phys. Rev.* **78**, 695 (1950).
 - [31] H. Lee, P. Kok, and J. P. Dowling, A quantum Rosetta stone for interferometry, *J. Mod. Opt.* **49**, 2325 (2002).
 - [32] C. L. Degen, F. Reinhard, and P. Cappellaro, Quantum sensing, *Rev. Mod. Phys.* **89**, 035002 (2017).
 - [33] A. Arias, A. Gheondea, and S. Gudder, Fixed points of quantum operations, *J. Math. Phys.* **43**, 5872 (2002).
 - [34] V. V. Albert, Asymptotics of quantum channels: Conserved quantities, an adiabatic limit, and matrix product states, *Quantum* **3**, 151 (2019).
 - [35] M. Bauer and D. Bernard, Convergence of repeated quantum nondemolition measurements and wave-function collapse, *Phys. Rev. A* **84**, 044103 (2011).
 - [36] W.-L. Ma, S.-S. Li, and R.-B. Liu, Sequential generalized measurements: Asymptotics, typicality, and emergent projective measurements, *Phys. Rev. A* **107**, 012217 (2023).
 - [37] P. Wang, W. Yang, and R. Liu, Using weak measurements to synthesize projective measurement of nonconserved observables of weakly coupled nuclear spins, *Phys. Rev. Appl.* **19**, 054037 (2023).
 - [38] H. Bernien, B. Hensen, W. Pfaff, *et al.*, Heralded entanglement between solid-state qubits separated by three metres, *Nature* **497**, 86 (2013).
 - [39] P. C. Maurer, G. Kucsko, C. Latta, L. Jiang, N. Y. Yao, S. D. Bennett, F. Pastawski, D. Hunger, N. Chisholm, M. Markham, *et al.*, Room-temperature quantum bit memory exceeding one second, *Science* **336**, 1283 (2012).
 - [40] J. Cai, A. Retzker, F. Jelezko, *et al.*, A large-scale quantum simulator on a diamond surface at room temperature, *Nature Physics* **9**, 168 (2013).
 - [41] M. H. Abobeih, Y. Wang, J. Randall, *et al.*, Fault-tolerant operation of a logical qubit in a diamond quantum processor, *Nature* **606**, 884 (2022).
 - [42] J. Randall, C. Bradley, F. van der Gronden, A. Galicia, M. Abobeih, M. Markham, D. Twitchen, F. Machado, N. Yao, and T. Taminiau, Many-body-localized discrete time crystal with a programmable spin-based quantum simulator, *Science* **374**, 1474 (2021).
 - [43] V. V. Soshenko, S. V. Bolshedvorskii, O. Rubinas, V. N. Sorokin, A. N. Smolyaninov, V. V. Vorobyov, and A. V. Akimov, Nuclear spin gyroscope based on the nitrogen vacancy center in diamond, *Phys. Rev. Lett.* **126**, 197702 (2021).
 - [44] M. Blok, C. Bonato, M. Markham, D. Twitchen, V. Dobrovitski, and R. Hanson, Manipulating a qubit through the backaction of sequential partial measurements and real-time feedback, *Nature Physics* **10**, 189 (2014).
 - [45] C. Bonato, M. S. Blok, H. T. Dinani, D. W. Berry, M. L. Markham, D. J. Twitchen, and R. Hanson, Optimized quantum sensing with a single electron spin using real-time adaptive measurements, *Nature nanotechnology* **11**, 247 (2016).
 - [46] A. Dréau, P. Spinicelli, J. R. Maze, J.-F. Roch, and V. Jacques, Single-shot readout of multiple nuclear spin qubits in diamond under ambient conditions, *Phys. Rev. Lett.* **110**, 060502 (2013).
 - [47] A. H. Burrell, D. J. Szwer, S. C. Webster, and D. M. Lucas, Scalable simultaneous multiqubit readout with 99.99% single-shot fidelity, *Phys. Rev. A* **81**, 040302 (2010).
 - [48] P. Neumann, J. Beck, M. Steiner, F. Rempp, H. Fedder, P. R. Hemmer, J. Wrachtrup, and F. Jelezko, Single-shot readout of a single nuclear spin, *science* **329**, 542 (2010).
 - [49] L. Childress, M. V. G. Dutt, J. M. Taylor, A. S. Zibrov, F. Jelezko, J. Wrachtrup, P. R. Hemmer, and M. D. Lukin, Coherent dynamics of coupled electron and nuclear spin qubits in diamond, *Science* **314**, 281 (2006).
 - [50] J. Meinel, V. Vorobyov, P. Wang, B. Yavkin, M. Pfender, H. Sumiya, S. Onoda, J. Isoya, R.-B. Liu, and J. Wrachtrup, Quantum nonlinear spectroscopy of single nuclear spins, *Nature Communications* **13**, 5318 (2022).
- Acknowledgments.** This work is supported by the Innovation Program for Quantum Science and Technology (Grants Nos. 2023ZD0300600, 2021ZD0302300), the National Key Research and Development Program of China (Grants No. 2023YFA1608900), the National Natural Science Foundation of China (Grant Nos. 12022509, 11934018, T2121001), and the Chinese Academy of Sciences (Grant Nos. YSBR90, YSBR-100, E0SEBB11, E27RBB11).
- Author contributions.** W.L.M and G.Q.L. conceived the project, J.X.Z conducted the experiments with the supervision of G.Q.L, Y.D.J and C.D.Q performed theoretical analysis and simulations with the supervision of W.L.M. All authors contributed to the writing of the paper.

Methods

Experimental setup and sample information.

The experiments are performed with a [100]-oriented, type IIa single-crystal diamond produced by Element Six, with a natural ^{13}C isotopic abundance of 1.1%. To improve the photon collection efficiency, a solid immersion lens (SIL) is etched onto the diamond surface. Under saturation conditions, the photon counting rate of the NV center is about 300 kcps. The diamond was mounted on a custom-built confocal microscope, and a 532-nm laser is used to initialize and read out the NV spin states. The laser pulses are generated with an acoustic optical modulator (AOM, Gooch & Housego 3350-199). The fluorescence emitted from the NV center is collected with the same objective, passed through a dichroic mirror and a 650-nm long-pass filter, then coupled into a multimode fiber and detected with a single photon detector (SPD). The fluorescence photons are counted with an NI-data acquisition card (NI-6343).

To control the NV electron spin and the ^{14}N nuclear spins, we use an arbitrary waveform generator (AWG, Tektronix 5024C) to generate transistor-transistor logic (TTL) signals and low-frequency analog signals. The synchronized TTL signals are used to control the AOM, RF switches and counters. For electron spin manipulation, the microwave (MW) carrier signal from a MW source (Rohde & Schwarz SMIQ03B) is combined with two analog AWG signals using an IQ-mixer (Marki Microwave IQ1545LMP). An additional analog signal is used to generate the RF signal for nuclear spin manipulation. Both the MW and RF signals are amplified by amplifiers (Mini Circuits, ZHL-16W-43-S+ and 32A-S+). The MW and RF signals are transmitted to the NV position via a gold co-planar waveguide deposited on the diamond surface.

As can be seen in the ODMR spectrum of the NV center, there is no splitting due to hyperfine interaction with strongly coupled ^{13}C nuclear spin, and a static magnetic field $B = 108.4 \pm 0.2$ G is applied close to the NV symmetry axis. The spin transition between the $|0\rangle_e \leftrightarrow |-1\rangle_e$ electronic spin states is addressed via microwave pulses. Figure S2 shows the free-induction decay (FID) signal of the measured NV center, which gives $T_{2e}^* = 2.9$ μs .

For the ^{14}N nuclear spin, the measurement strength oscillates as a function of the RIM duration τ . Considering the nuclear spin relaxation and the NV electron spin dephasing time, $\tau = 374$ ns is chosen to perform the experiments. Under these circumstances, the relaxation induced by sequential RIMs precedes the intrinsic ^{14}N nuclear spin T_1 process. For each RIM, an optical pulse of 220 ns is used to read out the population of the NV electron spin. After the first measurement, the nuclear spin randomly collapses to $|0\rangle_n$ or $|\pm 1\rangle_n$, and in the following measurement, it remains at the same state until a quantum jump occurs.

Quantum channels and their representations

Quantum channel, also called completely positive and trace-preserving (CPTP) map, describes the most general (closed or open) quantum dynamics that a quantum system can undergo. Each quantum channel has four different representations: the Kraus representation, the Stinespring representation, the natural representation, and the Choi representation. The Kraus representation is the most commonly used and characterizes a channel by a set of Kraus operators $\{M_a\}_{a=1}^r$, which satisfy $\sum_a M_a^\dagger M_a = \mathbb{I}$, such that $\Phi(\cdot) = \sum_{a=1}^r M_a(\cdot)M_a^\dagger = \sum_{a=1}^r \mathcal{M}_a(\cdot)$. The Stinespring representation is a dilation of a quantum channel, which is realized by coupling the bath system to a probe system, subjecting the composite system to a unitary evolution and then tracing over the probe system, i.e. $\Phi(\rho_n) = \text{Tr}_e[U(\rho_e \otimes \rho_n)U^\dagger]$, where $\text{Tr}_e[\cdot]$ denotes the partial trace over the probe qubit.

Since a quantum channel acts on the operator space of the bath system and can be considered as a superoperator, it is more convenient to use its natural representation in the Hilbert-Schmidt (HS) space. In the HS space, an operator is transformed into a vector ($X = \sum_{i,j=1}^d x_{ij}|i\rangle\langle j| \leftrightarrow |X\rangle\rangle = \sum_{i,j=1}^d x_{ij}|ij\rangle\rangle$), so that each superoperator is transformed into a single matrix ($X(\cdot)Y \rightarrow X \otimes Y^T$). Thus, the natural representation of Φ is $\hat{\Phi} = \sum_{a=1}^r \hat{\mathcal{M}}_a$ with $\hat{\mathcal{M}}_a = M_a \otimes M_a^*$. Note that we add hats on the operators of the HS space.

In the natural representation, we can spectrally decompose the quantum channel as

$$\hat{\Phi} = \sum_i \lambda_i |R_i\rangle\rangle\langle\langle L_i|, \quad (5)$$

where λ_i is the i th eigenvalue with the corresponding right (left) eigenvector $|R_i\rangle\rangle$ ($|L_i\rangle\rangle$), satisfying $\hat{\Phi} |R_i\rangle\rangle = \lambda_i |R_i\rangle\rangle$, $\hat{\Phi}^\dagger |L_i\rangle\rangle = \lambda_i^* |L_i\rangle\rangle$, and the biorthonormalization condition $\langle\langle L_i|R_j\rangle\rangle = \text{Tr}(L_i^\dagger R_j) = \delta_{ij}$ with δ_{ij} being the Kronecker delta. The eigenvalues $\{\lambda_i\}$ of a quantum channel are all located within a unit disk of the complex plane. The eigenspaces with $\lambda = 1$ are called *fixed points*, those with $\lambda = e^{i\varphi}$ and $\varphi \neq 0$ are rotating points, and those with $|\lambda| < 1$ are decaying points such that the information of such points collapses as $\hat{\Phi}^m |R_j\rangle\rangle = \lambda_j^m |R_j\rangle\rangle \rightarrow 0$ for $|\lambda_j| < 1$.

Metastability in sequential quantum channels

Of particular interest are the decaying points with eigenvalue $|\lambda_i| \approx 1$, which are called *metastable points*, and are denoted by $|\rho_{\text{fix}}^i\rangle\rangle$. Quantum metastability emerges when there are metastable points in the channel spectrum. Although the information of these metastable points will be finally lost, it can be well preserved within a certain range of m . Specifically, for the channel with r fixed points and $q - r$ metastable fixed points, the contributions of the metastable points cannot be neglected when $m \ll \mu' = 1/|\ln|\lambda_q||$, while the contribution of the other decaying points decays fast as m grows and can be omitted when $m \gg \mu'' = 1/|\ln|\lambda_{q+1}||$. So μ' and μ''

delimit a metastable region:

$$\frac{1}{|\ln |\lambda_{q+1}||} \ll m \ll \frac{1}{|\ln |\lambda_q||}. \quad (6)$$

When the eigenvalue of metastable points are very close to 1, and the decaying points relax fast, which is suitable for our case, the metastable region can be estimated as

$$m \ll \frac{1}{|\ln |\lambda_q||} \approx \frac{1}{1 - |\lambda_q|} \quad (7)$$

In the metastable region, $\lambda_i^m \approx 1$ for $i \leq q$ and $\lambda_j^n \approx 0$ for $j > q$, then we have

$$\hat{\Phi}^m |\rho\rangle \simeq \sum_{i=1}^r c_i |\rho_{\text{fix}}^i\rangle + \sum_{j=r+1}^q \tilde{c}_j |R_j\rangle, \quad (8)$$

for initial state $|\rho\rangle = \sum_i c_i |R_i\rangle$ with $\tilde{c}_j = c_j e^{im\varphi_j}$. We note that the metastable points, as decaying points, are trace-zero, so any metastable state in metastable manifold is a superposition of both fixed points (trace-1) and metastable points, denoted by $\{c_1, \dots, c_r, \tilde{c}_{r+1}, \dots, \tilde{c}_q\}$, with $\sum_{i=1}^r c_i = 1$, corresponding to a point in the $(q-1)$ dimensional HS subspace.

We can transform from the HS subspace to the metastable manifold (MM), which contains the metastable states as a convex combination of q extreme metastable states (EMSs)

$$|\rho_{\text{MS}}\rangle = \sum_{\nu=1}^q p_\nu |\rho_{\text{EMS}}^\nu\rangle \quad (9)$$

where $p_\nu = \langle P_\nu | \rho_{\text{MS}} \rangle$, P_ν is the projector to $|\rho_{\text{EMS}}^\nu\rangle$, i.e. $\langle P_\nu | \rho_{\text{EMS}}^\mu \rangle = \delta_{\nu\mu}$ and $\sum_\nu P_\nu = \mathbb{I}$, thus $\sum_\nu p_\nu = 1$, and EMSs are extremal points of the convex hull.

For the case of $r = 1$ and $q = 2$, i.e. the channel has one fixed point and one metastable point, forming a one-dimensional MM with the EMSs

$$|\rho_{\text{EMS}}^{1,2}\rangle = |\rho_{\text{fix}}\rangle + c_2^{M,m} |R_2\rangle / h, \quad (10)$$

where c_2^M (c_2^m) is the maximal (minimal) eigenvalue of L_2 , and $h = \sqrt{\langle L_2 | L_2 \rangle \langle R_2 | R_2 \rangle}$ is a normalization coefficient.

Metastability in sequential RIMs

The dynamics of the bath system after a RIM sequence of the probe is described by a quantum channel, which can be represented in the Stinespring representation as

$$\Phi(\rho_n) = \text{Tr}_e[U(\rho_e \otimes \rho_n)U^\dagger] \quad (11)$$

where $\rho_e = R_{\phi_1}(\frac{\pi}{2})|0\rangle_e \langle 0| R_{\phi_1}^\dagger(\frac{\pi}{2})$. For the Hamiltonian

$$H = \sigma_e^z \otimes B_n + \mathbb{I}_e \otimes C_n, \quad (12)$$

the unitary evolution can be decomposed as $U = e^{-iH\tau} = \sum_{\alpha=0,1} |\alpha\rangle_e \langle \alpha| \otimes U_\alpha$ with $U_\alpha = e^{-i[(-1)^\alpha B_n + C_n]\tau}$. After

taking the trace over the probe, the channel can be transformed to the Kraus representation as

$$\Phi(\rho_n) = \sum_{a=0,1} \mathcal{M}_a(\rho_n) = \sum_{a=0,1} M_a \rho_n M_a^\dagger, \quad (13)$$

where $\mathcal{M}_a(\cdot) = M_a(\cdot)M_a^\dagger$ is a superoperator with the Kraus operator $M_a = [U_0 - (-1)^a e^{i\Delta\phi} U_1]/2$ and $\Delta\phi = \phi_2 - \phi_1$ is the phase difference between the rotation axes of $R_{\phi_1}(\frac{\pi}{2})$ and $R_{\phi_2}(\frac{\pi}{2})$. Then the natural representation of the channel for the RIM case is

$$\hat{\Phi} = \hat{\mathcal{M}}_0 + \hat{\mathcal{M}}_1 = (\hat{U}_0 + \hat{U}_1)/2, \quad (14)$$

where $\hat{U}_\alpha = U_\alpha \otimes U_\alpha^*$, and $\hat{\mathcal{M}}_a = M_a \otimes M_a^*$.

We have proved that the spectrum of the quantum channel induced by RIM is determined by the commutativity of B_n and C_n . If $[B_n, C_n] = 0$, then B_n and C_n can be diagonalized simultaneously

$$B_n = \sum_{k=1}^d b_k |k\rangle \langle k|, \quad C_n = \sum_{k=1}^d h_k |k\rangle \langle k|. \quad (15)$$

The fixed points are spanned by all the rank-1 projectors $\{P_k\}_{k=1}^d$. While if $[B_n, C_n] \neq 0$, B_n and C_n can only be block diagonalized with a unitary transformation,

$$B_n = W \left(\bigoplus_{j=1}^r B_{n,j} \right) W^\dagger, \quad C_n = W \left(\bigoplus_{j=1}^r C_{n,j} \right) W^\dagger \quad (16)$$

where $r < d$ is the number of blocks. Such a block diagonalization partitions the Hilbert space of the bath system into a direct sum of r subspaces $\mathcal{H} = \bigoplus_{j=1}^r \mathcal{H}_j$. Then we prove that the fixed points in this case are spanned by all the projectors $\{\Pi_j\}_{j=1}^r$ to the blocks. Note that since $\text{rank}(\Pi_j) \geq 1$ and $r < d$, the number of bases for fixed points in the latter case is smaller than that of the former case. The decreasing of fixed points indicates the growth of decaying points.

However, we have proved that when C_n is a perturbation of B_n , i.e. $\|C_n\|/\|B_n\|$ is small, the emerged decaying points are actually metastable points and the EMSs of this case are approximately the eigenstates of B_n [6].

Model for the NV system

The full Hamiltonian for the system composed of the NV electron and the ^{14}N nuclear spin is

$$H = DS_z^2 + \gamma_e \mathbf{B} \cdot \mathbf{S} + \mathbf{S} \cdot \mathbb{A} \cdot \mathbf{I} + QI_z^2 + \gamma_n \mathbf{B} \cdot \mathbf{I}, \quad (17)$$

where \mathbb{A} is the hyperfine interaction tensor, containing only the zz -component $A_{zz}S_zI_z$ and the transverse component $A_\perp(S_xI_x + S_yI_y)$ for the ^{14}N nuclear spin. Since the large zero-field splitting of the NV electron spin suppresses the transition between $|m_s = 0\rangle$ and $|m_s = \pm 1\rangle$, the Hamiltonian Eq. (17) can be well approximated as a pure-dephasing form in Eq. (1) under the second-order perturbation [49].

Let $H_0 = DS_z^2 - \gamma_e B_z S_z + S_z A_{zz} I_z + QI_z^2 - \gamma_n \mathbf{B} \cdot \mathbf{I}$ and $H_1 = -\gamma_e (B_x S_x + B_y S_y) + A_\perp (S_x I_x + S_y I_y)$, then H_1 is a perturbation on H_0 . The second order perturbation gives $\tilde{H}_1 = \sum_\alpha |\alpha\rangle_e \langle\alpha| \otimes H_n^\alpha$, in which

$$H_n^\alpha = P_\alpha^e H_1 \frac{1}{E_\alpha - (\mathbb{I}_e - P_\alpha^e) H_0 (\mathbb{I}_e - P_\alpha^e)} H_1 P_\alpha^e, \quad (18)$$

with $E_\alpha = D\alpha^2 - \gamma_e B_z \alpha$. Specifically, we have

$$H_n^\alpha \approx \frac{\gamma_e(2-3|\alpha|)}{2D} [-\gamma_e(B_x^2 + B_y^2) + 2A_\perp(B_x I_x + B_y I_y)]. \quad (19)$$

In the rotating frame associated with $H_R = DS_z^2 + \gamma_e B_z S_z$, the Hamiltonian becomes

$$\begin{aligned} H &= e^{iH_R t} (H - H_R) e^{-iH_R t} \\ &= A_{zz} S_z I_z + QI_z^2 - \gamma_n \mathbf{B} \cdot \mathbf{I} + \tilde{H}_1, \end{aligned} \quad (20)$$

which is time-independent since $[H_R, \tilde{H}_1] = 0$ under the second-order perturbation. The above equation can be cast in the form of Eq. (12) with $B_n = A_{zz} I_z$ and $C_n = QI_z^2 - \gamma_n \mathbf{B} \cdot \mathbf{I} + \tilde{H}_1$.

When the magnetic field is perfectly aligned along the NV axis, $[B_n, C_n] = 0$, the fixed points of the channel are $P_\beta^n = |\beta\rangle_n \langle\beta|$, with $\beta = 0, \pm 1$. While when the magnetic field deviates slightly from the axis, $[B_n, C_n] \neq 0$, the channel has only one fixed point, which is the maximum mixed state $\mathbb{I}_n/3 = (P_1^n + P_0^n + P_{-1}^n)/3$, and two metastable points. The convex combination of the fixed point and the two metastable points spans a two-dimensional MM holding three EMSs, which are exactly P_β^m . We note that the eigenvalues λ_2 and λ_3 of two metastable points with eigenvalues are usually different ($|\lambda_2| > |\lambda_3|$), which makes it difficult to directly observe the three-peak feature in experiments. As m is so large that the contribution of one metastable point can be neglected ($|\lambda_3|^m \rightarrow 0$), the remaining metastable point, together with the fixed point, span a one-dimensional MM with two EMSs, which can be calculated by Eq. (10). For Fig. 2, numerical calculations show that the two observed EMSs are $\rho_D = P_1^n$ and $\rho_B = (P_0^n + P_{-1}^n)/2$.

Weak measurements of the probe spin

In this section, we model the optical readout process of NV centers at room temperature. If n photons are collected by the counter, the Kraus operator K_n acting on the NV electron spin is [50]

$$K_n = \sum_{\alpha=0,1} \sqrt{p(n|\alpha)} P_\alpha^e, \quad (21)$$

where P_α^e is projector on subspace α and collected photon numbers obey Poisson distribution $p(n|\alpha) = \frac{1}{n!} e^{-n_\alpha} n_\alpha^n$ with n_α being the average photon number obtained for state $|\alpha\rangle_n$. If n_α is small (about 0.05 in our experiments), truncating to K_0 and K_1 is a good approximation with $p(1|\alpha) = n_\alpha$ and $p(0|\alpha) = 1 - p(1|\alpha)$.

Then the Kraus operator on the ^{14}N bath spin when obtaining n photons can be derived as

$$\begin{aligned} W_n(\rho) &= \text{Tr}_e [K_n R_2 U R_1 (|0\rangle_e \langle 0| \otimes \rho) R_1^\dagger U^\dagger R_2^\dagger K_n^\dagger] \\ &= \sum_{\alpha=0,1} p(n|\alpha) M_\alpha \rho M_\alpha^\dagger, \end{aligned} \quad (22)$$

where $M_\alpha = [U_0 - (-1)^\alpha e^{i\Delta\phi} U_1]$ is the Kraus operator introduced in Eq. (2), which corresponds to perfect projective measurements. Note that

$$\begin{aligned} \hat{\Phi}' &= \sum_n \hat{W}_n = \sum_{\alpha=0,1} \sum_n p(n|\alpha) \hat{M}_\alpha \\ &= \hat{\Phi}, \end{aligned} \quad (23)$$

then the channel with the set of Kraus operators $\{W_n\}_{n=0}^\infty$ is the same as that with $\{M_\alpha\}_{\alpha=0,1}$, so the analysis of the channel decomposition in the section above also applies here.

Measurement statistics of sequential RIMs.

The fixed points (or metastable points) can be observed by the measurement statistics of sequential RIMs. A single RIM includes the measurement on the probe spin with an outcome $a \in \{0, 1\}$, while for sequential RIMs we obtain a sequence of binary numbers $\{a_1, \dots, a_m\}$. This sequence of measurement outcomes defines a quantum trajectory. We then look for some statistical observable which can characterize different quantum trajectories and their corresponding fixed points.

In practice, we often focus on the average of the m measurement results and its expectation, i.e., $\bar{a} = \frac{1}{m} \sum_{n=1}^m a_n$, which in our case coincides with f_1 and can be related to the measurement polarization by $X = 1/2 - f_1$. The expectation of measurement average can be written as

$$\langle f_1 \rangle = \sum_{a_1} \dots \sum_{a_m} f_1 p(a_1, \dots, a_m | \rho), \quad (24)$$

where the probability to get a specific sequence of measurement results $\{a_1, \dots, a_m\}$ is given by

$$p(a_1, \dots, a_m | \rho) = \left\langle \left\langle \mathbb{I} | \hat{\mathcal{M}}_{a_m} \dots \hat{\mathcal{M}}_{a_1} | \rho \right\rangle \right\rangle. \quad (25)$$

It can be shown that in the asymptotic limit, i.e., when number of repetitions is large enough $m \rightarrow \infty$, $\langle f_1 \rangle$ is only determined by fixed points,

$$\lim_{m \rightarrow \infty} \langle f_1 \rangle = \sum_{j=1}^J c_j \langle f_{1j} \rangle_*, \quad (26)$$

where we assume there are J fixed points, with

$$\langle f_{1j} \rangle_* = \left\langle \left\langle \mathbb{I} | \hat{\mathcal{M}}_1 | \rho_{\text{fix}}^j \right\rangle \right\rangle = p(1 | \rho_{\text{fix}}^j), \quad (27)$$

where $c_j = \text{Tr}(\rho_{\text{fix}}^j \rho)$ amounts to the probability of obtaining j th fixed point given initial state ρ , and note the

second equation indicates that the expectation of measurement average coincides with the probability of obtaining result $a = 1$ for the fixed point ρ_{fix}^j in a single RIM,

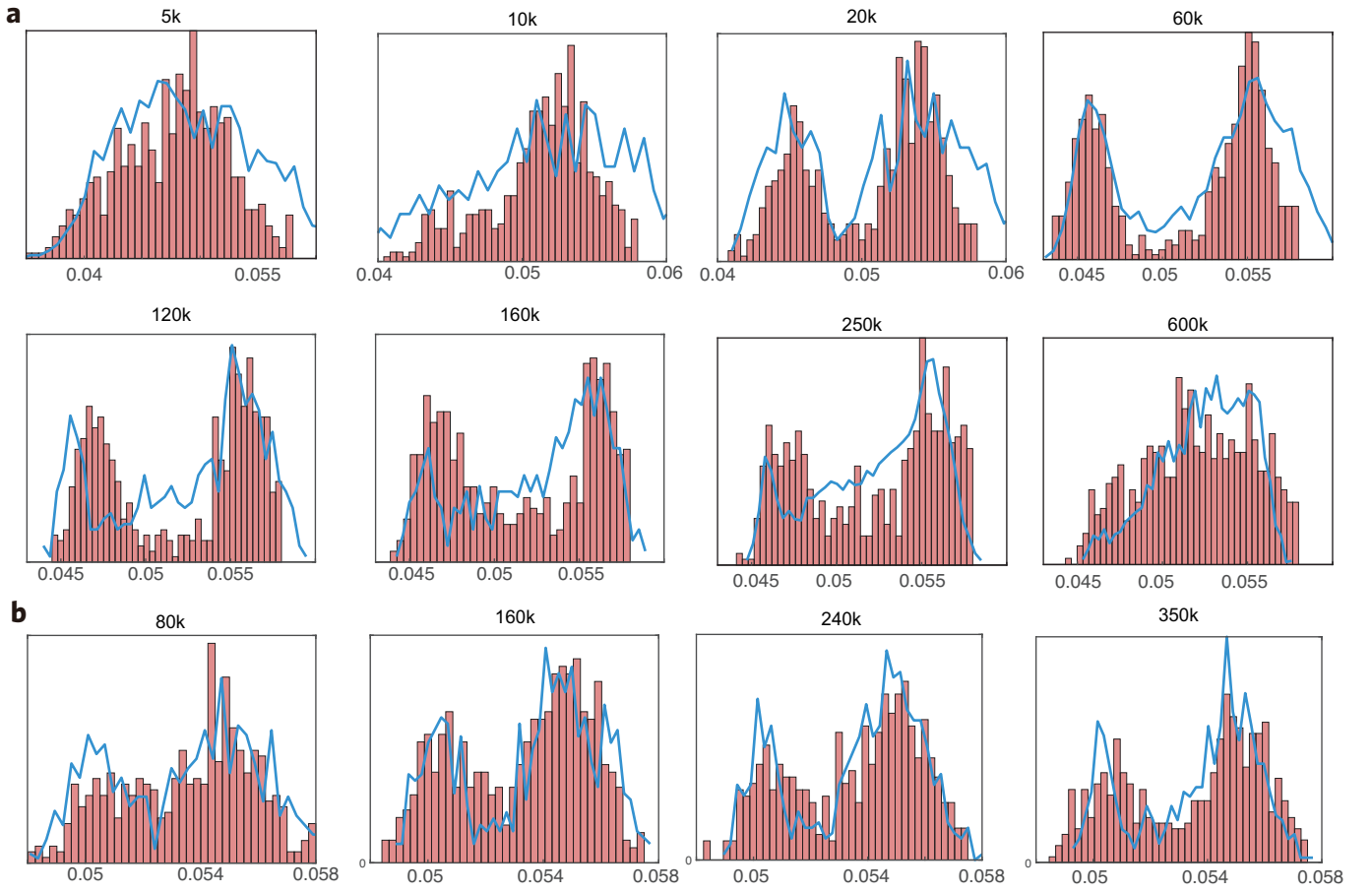
$$p(a|\rho) = \text{Tr}(M_a \rho M_a^\dagger) = \left\langle \left\langle \mathbb{I} | \hat{\mathcal{M}}_a | \rho \right\rangle \right\rangle. \quad (28)$$

In other words, the distribution of the measured frequency can have J peaks (without degeneracy), each centered around the expectation determined by each fixed point $\{\langle f_{1j} \rangle_*\}_{j=1}^J$ respectively. Each peak includes trajectories defined by $\{a_1, \dots, a_m\}$ with a frequency f_1 close to $\langle f_{1j} \rangle_*$, which can steer any initial state to one of the fixed point subspaces [36].

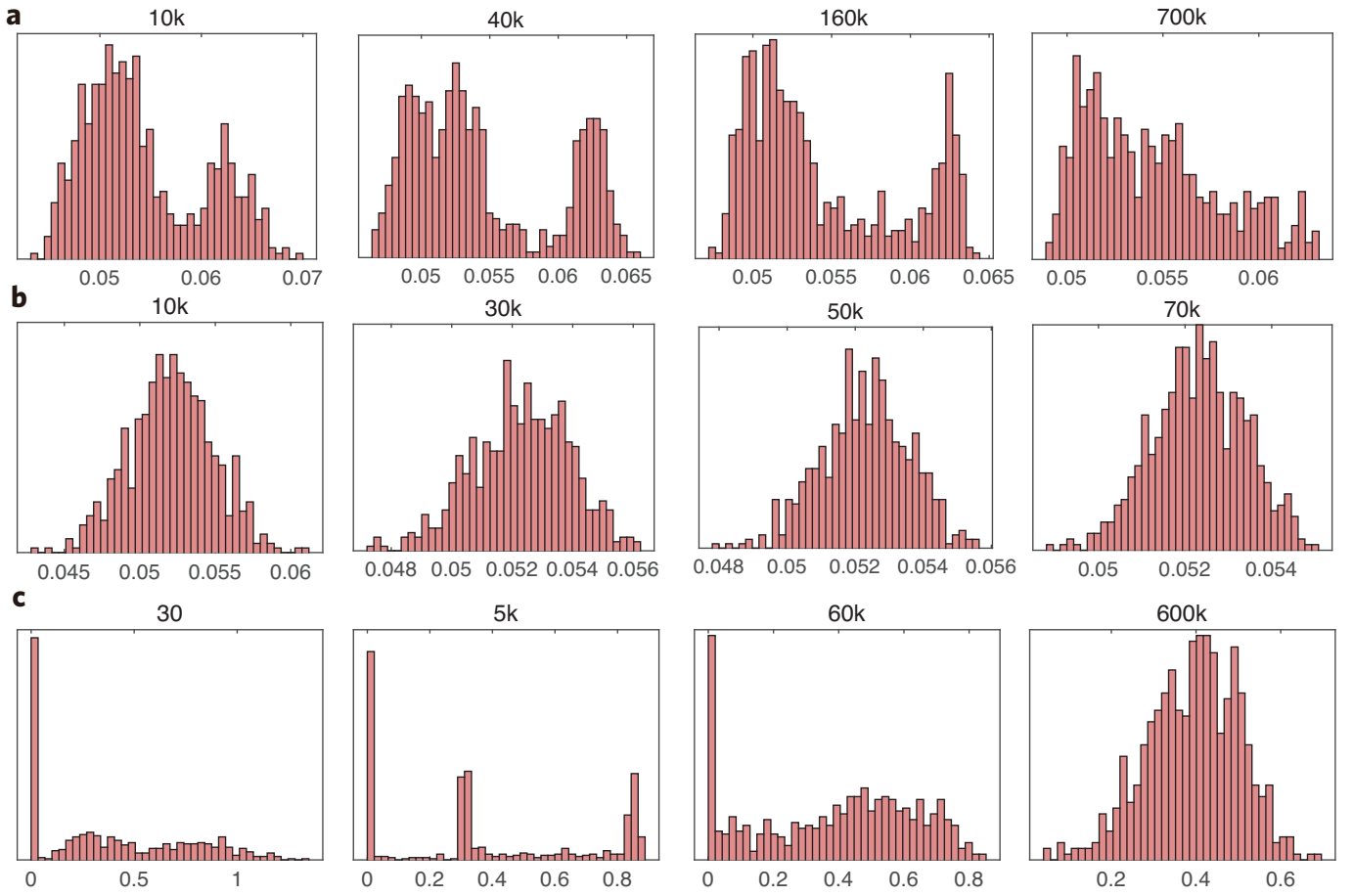
Taking into account the weak measurements, the average photon number corresponding to the j th fixed (metastable) point is

$$\begin{aligned} \langle n_j \rangle_* &= \sum_n \langle \langle \mathbb{I} | n \hat{\mathcal{W}}_n | \rho_{\text{fix}}^j \rangle \rangle \\ &= \sum_{n, \alpha} n p(n|\alpha) \langle f_{\alpha j} \rangle_* \end{aligned} \quad (29)$$

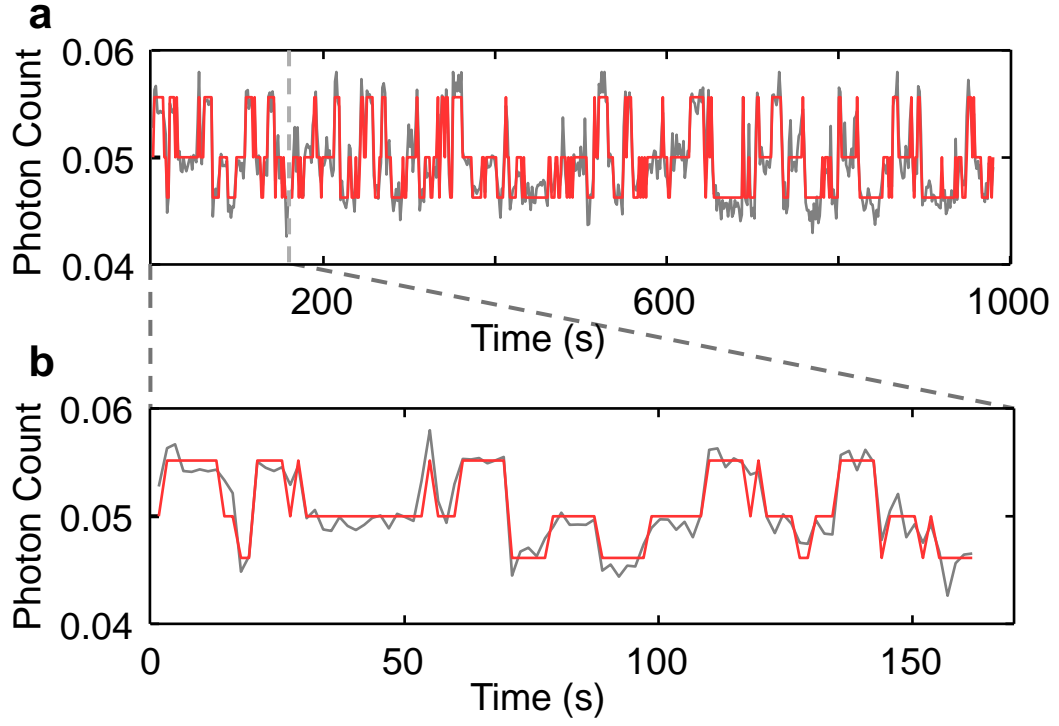
in which $\hat{\mathcal{W}}_n = W_n \otimes W_n^* = \sum_{\alpha=0,1} p(n|\alpha) \hat{\mathcal{M}}_\alpha$ is the superoperator of W_n in the HS space.



Extended data Fig. 1. **a**, Statistical results of the PL trace of the experiment with field tilt angle $7^\circ \pm 2^\circ$ and $\tau = 374$ ns, data of 5 k, 60 k, 250 k, 600 k are shown in Fig. 2c). **b**, another experiment with the field tilt angle of $8^\circ \pm 2^\circ$ and $\tau = 370$ ns, the distribution of consecutive measurements in experiment (red histogram) and simulation (blue fitting line). The simulation in **b** is performed under $\theta = 7.94^\circ$, which is close to the angle in the experiment.



Extended data Fig. 2. Histogram of the results of the Monte Carlo simulation. The parameters of **a-b** are **a** $\theta = 3.5^\circ$ and **b** $\theta = 15^\circ$ with weak measurement ($n_0 = 0.065$ and $n_1 = 0.049$). **c**, numerical simulation results with strong measurement ($n_0 = 0$ and $n_1 = 1$) with $\theta = 8.8^\circ$



Extended data Fig. 3. Triple-peak quantum jumps. **a**, With a slight misalignment of the magnetic field with respect to the NV axis, the signal of triple-peak quantum jumps is observed at the RIM duration $\tau = 350$ ns, $m = 60$ k. The red fitting line is extracted from the HMM model. **b**, The first 100 points of of triple-peak quantum jumps signal.